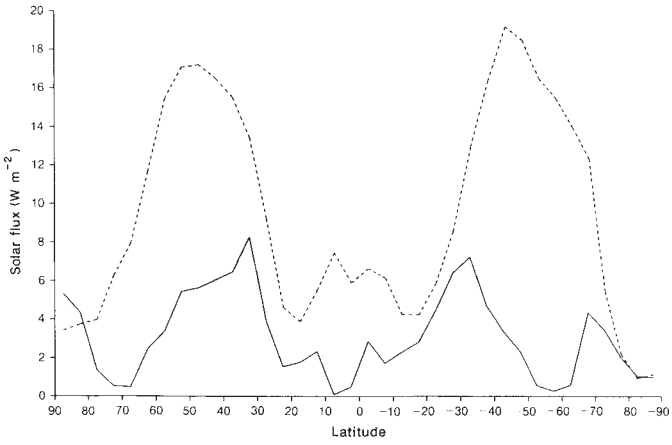

FIG. 4 Zone-averaged equilibrium change in net solar flux at the top of the atmosphere on doubling CO_2 (five-year mean). Solid line, simulation with CW. Dashed line, simulation with RH.

allow the cloud radiative properties to depend on the cloud water content (scheme CWRP). (Given the similarity between CW and CWH, this experiment was carried out with the CW formulation only.) Analytical fits of the short-wave albedo and transmittance as functions of cloud-water path and solar zenith angle were made to a published scheme[17] based on observations and theoretical considerations. The long-wave flux emittance was given by $(1-\exp(-\kappa q))$ where q is the condensed-water path and $\kappa = 0.13\ m^2\ g^{-1}$ for water clouds and $0.065\ m^2\ g^{-1}$ for ice clouds[18].

On doubling the CO_2 concentrations the global annual average equilibrium surface temperature increased by 1.9 K with CWRP compared to 2.7 K with prescribed cloud radiative properties (CW), indicating a further increase in λ to $2.1\ W\ m^{-2}\ K^{-1}$. This negative feedback from changes in cloud radiative properties lies between the very strong negative feedback suggested by one-dimensional calculations[16,19] and the positive feedback found in a previous study with a low-resolution general-circulation model (GCM)[4-6]. We note that all existing numerical studies assume that the number of CCN remains constant under climate change. Changes in CCN are a further possible source of feedback[7,20].

The sensitivity of the climate to doubling the CO_2 concentrations that we have found is substantially smaller than the 4-5 K found in other recent studies[10,21]. A significant part of this reduction in sensitivity is due to the different cloud scheme. If correct this will have two important consequences. First, the equilibrium warming expected from the estimated $2\ W\ m^{-2}$ increase in radiative heating at the tropopause since 1860 (ref. 9) will be smaller. Second, the proportion of the equilibrium reached will be greater, because the thermal response time of the climate system is reduced if climate sensitivity is reduced[22]. Based on calculations using a simple one-dimensional model of the ocean, the expected warming to date, using the climate sensitivity found when employing CW, is 0.6 K. This is close to the observed warming since the beginning of the century (0.5 K; ref. 23). The record of observations shows considerable variability on interannual and interdecadal timescales, however, including a period of cooling during the 1950s and 1960s, so that it is not possible to attribute the 0.5 K rise unambiguously to the effect of increases in trace gases. □

Received 14 June; accepted 14 August 1989.

1. Manabe, S. & Wetherald, R. T. *J. atmos. Sci.* **24,** 241-259 (1967).
2. Schneider, S. H. *J. atmos. Sci.* **29,** 1413-1422 (1972).
3. Wetherald, R. T. & Manabe, S. *J. atmos. Sci.* **45,** 1397-1415 (1988).
4. Roeckner, E. *et al. Nature* **329,** 138-140 (1987).
5. Roeckner, E. *Nature* **335,** 304 (1988).
6. Schlesinger, M. E. *Nature* **335,** 303-304 (1988).
7. Charlson, R. J. *et al. Nature* **334,** 418-420 (1988).
8. Mitchell, J. F. B. & Warrilow, D. A. *Nature* **330,** 238-240 (1987).
9. Smith, R. N. B. *Q. Jl R. met. Soc.* (in the press).
10. Dickinson, R. E. & Cicerone, R. J. *Nature* **319,** 109-115 (1985).
11. Wilson, C. A. & Mitchell, J. F. B. *J. geophys. Res.* **92,** 13,315-13,343 (1987).
12. Pruppacher, H. R. & Klett, J. D. *Microphysics of Cloud and Precipitation.* (Reidel, Dordrecht, 1978).
13. Heymsfield, A. J. & Sabin, R. M. *J. atmos. Sci.* **46,** 2252-2264 (1989).
14. Heymsfield, A. J. *J. atmos. Sci.* **34,** 367-381 (1977).
15. Mason, B. J. *The Physics of Clouds* (Clarendon, Oxford, 1957).
16. Somerville, R. C. J. & Remer, L. A. *J. geophys. Res.* **89,** 9668-9672 (1984).
17. Liou, K.-N. & Wittman, G. D. *J. atmos. Sci.* **36,** 1261-1273 (1979).
18. Stephens, G. L. *J. atmos. Sci.* **35,** 2123-2132 (1978).
19. Somerville, R. C. J. & Iacobellis, S. *Am. Met. Soc. 7th Conf. Ocean-Atmos. Interaction* 53-55 (1988).
20. Liou, K.-N. & Ou S.-C. *Preprints of 10th Int. Cloud Phys. Conf.* Vol. II, 118-120 (1988).
21. Schlesinger, M. E. & Mitchell, J. F. B. *Rev. Geophys.* **25,** 760-798 (1987).
22. Hansen, J. E. *et al. Geophysical Monographs Series* Vol. 29, 130-163 (American Geophysical Union, Washington, DC, 1984).
23. Jones, P. D. *et al. Nature* **338,** 790 (1988).

ACKNOWLEDGEMENTS. We would like to thank R. Smith who devised and wrote the cloud water scheme used.

Disequilibrium silicate mineral textures: fractal and non-fractal features

Anthony D. Fowler*, H. Eugene Stanley† & Gérard Daccord‡

* Ottawa-Carleton Geoscience Centre, University of Ottawa, Ottawa, Ontario, Canada K1N 6N5
† Center for Polymer Studies and Department of Physics, Boston University, Boston, Massachusetts 02215, USA
‡ Dowell Schlumberger, Z.I. Molina, BP 90, 42003 St Etienne, Cedex 1, France

IGNEOUS rocks formed from lava flows of the Archaean era (>2,700 million years ago) are often found to contain disequilibrium-textured crystals characterized by spherulitic, branching or dendritic morphologies that occur in layers near the flow surface. Well-known examples are the plagioclase spherulites of basalts and the platy and branching spinnifex-textured olivines and pyroxenes of komatiites[1,2]. Here we present evidence that, over a finite range of length scales, some disequilibrium textures are scale invariant. This observation implies that over this range of length scales their random patterns can be quantitatively characterized by a unique number, the fractal dimension[3]. We also demonstrate that some textures have a crossover from fractal to non-fractal behaviour. It is known that most disequilibrium crystals arise in part from rapid cooling and represent the case where the growth rates of the crystals are large compare to the diffusion rates in the silicate melt[1,2,4]. We therefore formulate a quantitative model for the growth that is based on a variant of diffusion-limited aggregation (DLA)[5].

Figure 1 shows a section of small disequilibrium crystals, at different magnifications. These form close to the quench/glassy margin of some lava flows[6], and their outline remains the same as the microscope objective power is increased. Similar remarks can be made about textures on other length scales, such as the much larger branching pyroxene crystal of Fig. 2*a*.

The concepts and techniques of fractal geometry[3] have proven useful in understanding other random morphologies, in part because a fractal object is characterized quantitatively by a number, the fractal dimension d_f, that relates the increase in mass M of the object to its characteristic length scale L, $M \approx L^{d_f}$ (ref. 7).

To determine d_f we digitized photographs of the textures using a video camera with a grid of 65,536 pixels. First we randomly chose any pixel belonging to the digitized texture. About this 'local origin' we constructed a sequence of concentric shells of

radius r. For each shell, we formed the correlation function $\mathscr{C}(r)$ by dividing the number of pixels belonging to the texture by the total number of pixels in that shell. To obtain good statistics we repeated the calculation using all texture pixels as local origins.

The correlation function $\mathscr{C}(r)$ gives the probability that a pixel separated from the local origin by a distance r is part of the pattern. We expect this function to scale in the same way as the density of pixels in a two-dimensional fractal object[7].

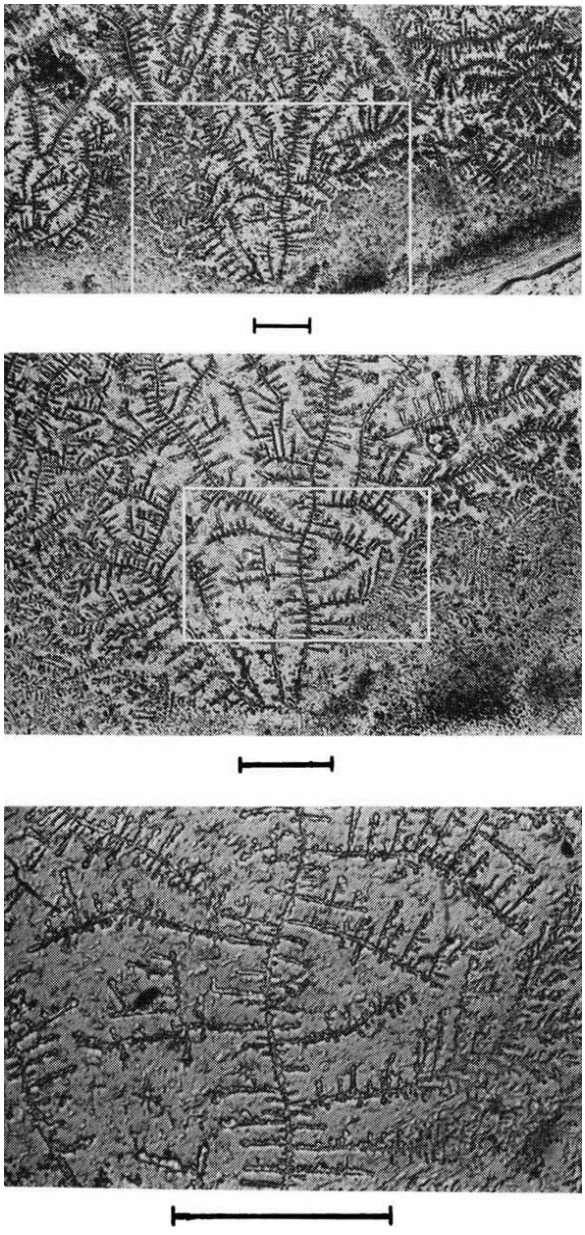

FIG. 1 Photomicrographs taken at increasing magnifications of the same field, of branching crystals (interpreted to be olivine) sampled from beneath the quenched pillow margin of an Archaean metabasalt flow. The scale bars represent a length of 0.1 mm. The enclosed areas indicate the field of view of the subsequent image. The branching pattern is independent of magnification; this scale invariance is characteristic of fractal objects. The images were taken using Nomarski interference microscopy of acid-etched samples[15]. Pillows may form during subaqueous eruption when lava in contact with water quickly quenches to a glass. The glass remains plastic and deforms under pressure of the flow into a bulbous shape (pillow) in a manner analogous to blown glass, except that the interior is lava filled. The pillows often contain a spectrum of mineral growth morphologies from the glassy margin to the slowly cooled pillow centre (~0.5 m).

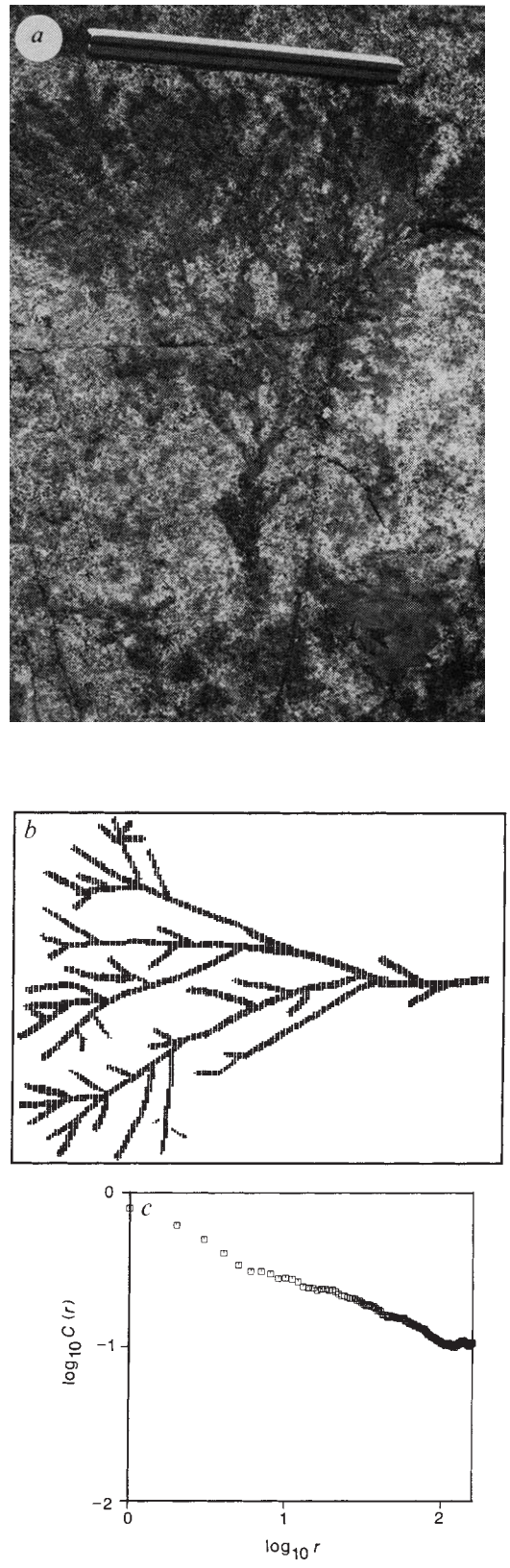

FIG. 2 *a*, Photograph of a large (scale = 32 cm) branching pyroxene from a gabbro sill in Munro Township of the Archaean Abitibi Subprovince, Ontario. These branching crystals are most evident on weathered surfaces and are exposed over several hundred metres of the sill in a haphazard manner. Elsewhere, such as at the location of the photo, their long axes are normal to cooling contacts. The crystal is clearly scale invariant and fractal in form. *b*, is the digitized form and *c*, shows that $d_f = 1.60 \pm 0.10$.

That is, the number of pixels that form part of the object is not proportional to the square of r but to the power d_f,

$$\mathscr{C}(r) \approx r^{d_f-2} \quad (1)$$

Thus the slope of a double logarithmic plot of $\mathscr{C}(r)$ against r gives a quantitative value of d_f.

Figure 3*a* shows a digitized version of the olivine of Fig. 1. Figure 3*b* is a double logarithmic plot of $\mathscr{C}(r)$ against r, and shows that for r less than a crossover value r_c of about 70 pixels, the data fall on a line of slope -0.20, corresponding to $d_f = 1.80 \pm 0.05$. For $r > r_c$, $\mathscr{C}(r)$ has a constant 'saturation' value $\mathscr{C}_{sat}$; hence over this range the object is non-fractal. We can check the numerical value of $\mathscr{C}_{sat}$ by calculating the mean density of the pattern; we find 6,682 black pixels in a total area of $222 \times 201 \approx 44{,}000$. Hence we expect $\log \mathscr{C}_{sat} \approx \log(0.15) \approx -0.82$ indicating that the initial concentration of olivine 'components' in the liquid was on the order of 15% in accordance with measured estimates of the sum of the contents of FeO and MgO of the rock[6].

We analysed at least a dozen additional crystals and consistently found evidence for their fractal nature below a crossover radius r_c. For example, the pyroxene (Fig. 2) has $d_f = 1.60 \pm 0.10$. The larger statistical uncertainty is due to the fact that outcrop weathering has somewhat obscured the outline of the crystal.

Experimental studies have clearly documented the conditions responsible for the growth of disequilibrium silicate crystals, but an understanding of the physical mechanisms remains obscure. We note that the fractal dimensions we find are similar to those found for DLA. The DLA algorithm starts with a seed particle and releases a random walker from the periphery of a circle enclosing the seed. When the random walker touches the seed, it sticks and a second walker is released. This process is iterated until a large aggregate is formed. The random walkers in DLA correspond to structural units in the silicate melt which undergo Brownian motion and upon collision attach to a central nucleus without rearrangement. The model is thus somewhat analogous to crystal growth in a magma under conditions of high supercooling. Protuberances preferentially grow because the probability is small that a molecule in a highly supercooled liquid will travel without collision into the 'fjords' between the branches of the crystals.

These disequilibrium crystals share other characteristics with DLA in addition to having a similar value of the fractal dimension. For example, they display a ramified (branched) structure, starting from a unique seed. Moreover, the branches do not form any 'closed loops'. A main difference between the DLA model and actual physical agglomeration processes is that the concentration of particles tends to zero in the DLA model. In any physical system, however, there is a finite concentration of molecules. This leads to the possibility that growth can occur in several different places at the same time. The effect[8] of deviation from this limiting condition of zero concentration on the structure of the final patterns is the crossover from fractal behaviour at small length scales to non-fractal (that is, constant density) behaviour at larger length scales. The characteristic length at which this crossover occurs depends on the concentration of particles and seeds.

Figure 4 shows the results of a 'finite-concentration' simulation, with the added feature that anisotropy has been introduced. Several seed particles are introduced and a non-zero concentration of walkers is distributed at random. At each time step, each walker attempts to move to one of its four neighbouring sites (chosen at random). If the neighbouring site is empty, the move is allowed, otherwise the move is prohibited. When a walker steps on a perimeter site of any cluster, it sticks irreversibly.

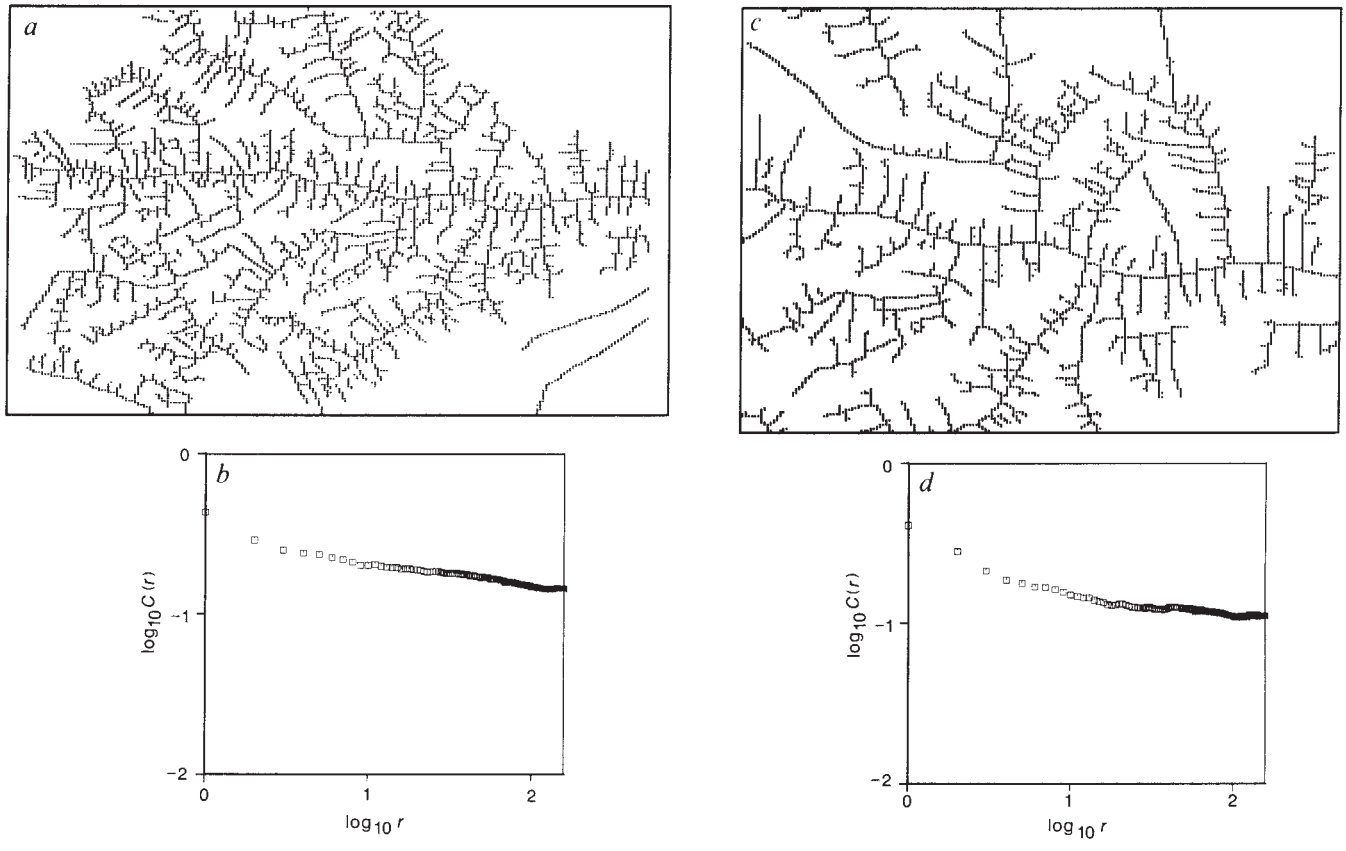

FIG. 3 *a*, Digitized representation of the central area of Fig. 1*a*. *b*, The graph of the correlation function as a function of length is characteristic of fractal forms and yelds $d_f = 1.80 \pm 0.05$. *c* and *d*, The digitized forms of the central area of Fig. 1*b* and the graph of correlation function as a function of length respectively, $d_f = 1.72 \pm 0.07$. Note that the fractal dimensions d_f of the two images are almost identical under change of scale.

Anisotropy is present in disequilibrium-crystal growth. The anisotropy is assumed to start when the fastest growing face of the crystal nucleus is aligned with the thermal or compositional gradient. Once initiated, the preferred direction is conserved as the crystals grow out from the depleted area in the direction of highest concentration, normal to the cooling contact. We have incorporated anisotropy in our model by introducing a local noise reduction. In conventional global noise reduction, a particle sticks after visiting a perimeter site s times (see, for example, ref. 9). In contrast, for local noise reduction, the parameter s has a lower value for perimeter sites co-linear with cluster sites; for the simulation of Fig. 4, we chose $s=1$ for perimeter sites aligned with the previous direction of growth and $s=2$ for the remaining perimeter sites.

The similarity of the olivine photographs (Fig. 1) and the simulation (Fig. 4) is rather striking, both qualitatively and quantitatively (they have roughly the same value of d_f, followed at a larger distance by a crossover to constant mass density). At small radii the short distance between tips of the mineral relative to the diffusion length of the molecules prevents in-filling, whereas at larger radii in the presence of a finite number of molecules the diffusion length is short with respect to tip distance so in-filling growth becomes more probable.

Although the stochastic model presented, DLA, provides us with a physical mechanism of growth, it yields no quantitative information about the actual mineral growth. A kinetic model that is a variant of DLA may be used, however, to calculate parameters associated with the growth of the olivine at the crossover. We use the Smoluchowski formulation, a theory of anomalous reaction kinetics that accounts for diffusion-limited growth. We base our analysis on the finding[8] that this crossover is entirely due to the finite concentration of particles. When the crossover occurs, the average displacement of a particle during a period of time δt equal to the mean time between two particles sticking on the cluster is of the order of the size of the cluster,

$$\sqrt{D\,\delta t} = r_c \tag{2}$$

To calculate δt we assume a given diffusivity D for the particles and thereby obtain an estimate of the particle concentration and other physical parameters.

We assume the flux of particles sticking on the cluster is the same as if the cluster were a filled sphere of size R; this assumption has been verified to hold for DLA[10], provided R is equal to an effective radius of the DLA cluster. This effective radius is smaller than the DLA actual outer radius but of the same order of magnitude. Therefore we use the expression of the flux of incoming particles toward a spherical sink[11,12]

$$\phi = 4\pi DRC\left(1+\frac{R}{\sqrt{\pi Dt}}\right) \tag{3}$$

where ϕ is the flux (number of particles per unit of time), R the cluster radius (effective radius of the DLA cluster), C the particle concentration far from the cluster and t the time since the beginning of the growth.

For DLA simulations the mean time between growth events δt corresponds to an increase in branch length equal to the particle size. The mean branch width for DLA is almost equal to the particle size[13]. Although the branch width W of real physical objects such as the minerals discussed here remains essentially constant, W^3 is much larger than the size of an individual molecule. Hence the corresponding mean time δt required to increase the branch length by W is simply $1/\phi$ multiplied by the number of molecules A, in a cube of volume W^3 of the mineral. Thus

$$\delta t = \frac{A}{\phi} \tag{4a}$$

and

$$A = W^3(\rho/M)N_A \tag{4b}$$

where ρ and M are the mineral density and relative molecular mass respectively, and N_A is Avogadro's number. For long times (for example, the time t required to reach $R=r_c$), equation (3) reduces to $\phi = 4\pi Dr_cC$ and from equation (4a)

$$\delta t \simeq \frac{A}{4\pi Dr_cC} \tag{5}$$

The concentration of species at the crossover may be calculated because $\delta t = r_c^2/D$ from equation (2). Thus equation (5) becomes

$$C \simeq \frac{A}{4\pi r_c^3} \tag{6}$$

From Fig. 3b we see that $r_c = 67$ pixels, which corresponds to 0.022 cm in Fig. 3a. Because a branch width is one pixel, $W = r_c/67 = 3.3\times10^{-4}$ cm. Using equation (4b), we obtain $A = 4.25\times10^{11}$ molecules. Hence from equation (6), $C = 3\times10^{15}$ molecules cm^{-3}. Using $D = 5\times10^{-7}$ cm^2 sec^{-1}, we calculate from equation (5) that the time δt of growth at the crossover is 970 s, yielding an instantaneous growth rate of 3.4×10^{-7} cm s^{-1}, similar to that reported[14] for skeletal olivine growth. Because the growth rate of DLA slows with growth, our value is a lower bound.

These results should be considered only as order of magnitude estimates because we have used very rough assumptions, the most critical of which is the use of equation (3). In the absence of any quantitative theory for DLA, however, we could not find an alternative approach. □

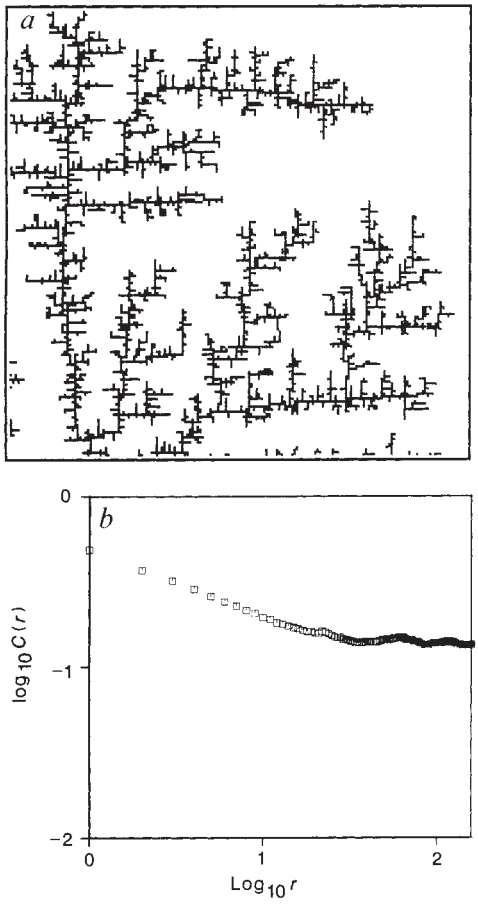

FIG. 4 *a*, Pattern simulated using the algorithm of ref. 8 modified to include local noise reduction ($s=2$ here). Of a total of 32,400 available pixels, 4,512 were selected as mobile particles. Only the central part of the simulation is illustrated because of boundary effects. *b*, The plot of the density correlation function, showing that in the fractal region $d_f = 1.73$. The crossover to non-fractal behaviour occurs at $r \approx 30$.

Received 25 August 1988; accepted 7 August 1989.

1. Lofgren, G. *Am. J. Sci.* **274,** 243–273 (1974).
2. Donaldson, C. H. *Contr. Miner. Petrol.* **57,** 187–213 (1976).
3. Mandelbrot, B. B. *The Fractal Geometry of Nature* (Freeman, New York, 1983).
4. Keith, H. D. & Padden, F. J. Jr *J. appl. Phys.* **34,** 2409–2421 (1963).
5. Witten, T. A. & Sander, L. M. *Phys. Rev. Lett.* **47,** 1400–1403 (1981).
6. Fowler, A. D., Jensen, L. S. & Peloquin, A. S. *Can. Mineralogist* **25,** 275–289 (1987).
7. Stanley, H. W. *Fractals and Multifractals: An Introduction* (Oxford University Press, in the press).
8. Witten, T. A. & Meakin, P. *Phys. Rev.* B**28,** 5632–5642 (1983).
9. Nittmann, J. & Stanley, H. E. *Nature* **321,** 663–668 (1986).
10. Yang, C.-L., Chen, Z.-Y. & El-Sayed, M. A. *J. phys. Chem.* **91,** 3002–3006 (1987).
11. Collins, F. C. & Kimball, G. E. *J. Colloid Sci.* **4,** 125–137 (1949).
12. Rice, S. A. *Diffusion-Limited Reactions* (Elsevier, New York, 1985).
13. Daccord, G. *Phys. Rev.* A**39,** 1365–1368 (1989).
14. Donaldson, C. H. *Lithos* **8,** 163–174 (1975).
15. CLark, A. H., Pearce, T. H., Roeer, P. L. & Wolfson, I. *Am. Miner.* **71,** 734–741 (1986).

ACKNOWLEDGEMENTS. We thank R. Ernst, R. Kretz, G. Lofgren & J. Veizer for providing constructive criticism and T. H. Pearce for access to the Nomarski microscope at Queen's University. We acknowledge the financial support of the University of Ottawa Development Fund, the Natural Science and Engineering Research Council of Canada, the NSF and the Office of Naval Research.

Carbon isotopes in soils and palaeosols as ecology and palaeoecology indicators

T. E. Cerling, J. Quade, Y. Wang & J. R. Bowman

Department of Geology and Geophysics, University of Utah, Salt Lake City, Utah 84112, USA

THERE are few quantitative techniques in use today for palaeoecological reconstruction in terrestrial depositional systems. One approach to such reconstructions is to estimate the proportion of C_3 to C_4 plants once present at a site using carbon isotopes from palaeosol carbonates[1–3]. Until now, this has been hampered by an inadequate understanding of the relationship between the carbon isotopic composition of modern soil carbonate and coexisting organic matter. Here we have found that the two systematically differ by 14–16‰ in undisturbed modern soils. This difference is compatible with isotopic equilibrium between gaseous CO_2, and aqueous and solid carbonate species in a soil system controlled by diffusive mass transfer of soil CO_2 derived from irreversible oxidation of soil organic matter. Organic matter and pedogenic carbonate from palaeosols of Pleistocene to late Miocene age in Pakistan also differ by 14–16‰. This indicates that diagenesis has not altered the original isotopic composition of either phase, thus confirming their use in palaeoecological reconstruction.

Stable carbon isotopes in pedogenic carbonate[1–4] and soil organic matter[5,6] can be used as palaeoecological indicators. A critical assumption, however, in the use of pedogenic carbonate is that of isotopic equilibrium between the carbon species—soil CO_2, dissolved carbonate species, and solid carbonate—in the soil system buffered by an effectively infinite soil CO_2 reservoir. Other studies in recent years have invoked processes such as 'Rayleigh' distillation[7,8], kinetic fractionation[8], and partial exchange or inheritance[8,9] to describe carbon isotope systematics in soils. The principal drawback of the latter models is that little isotope data on co-genetic organic carbon and soil carbonate was collected. Instead, the isotopic composition of the organic matter was usually assumed[7–9]. Where measured, the results were considered unreliable because of the vegetation changes resulting from cultivation[8]. Many of the studied soils have complex vegetational histories attributable to either the effects of cultivation and extensive grazing[7–9] or, in the case of calcretes[7], to long periods of development in the presence of pre-Holocene vegetation. These complexities make interpretation of the soil isotope system exceedingly difficult.

Our approach is to study ten soils in North America with simple pedogenic histories (Table 1). All the soils are latest Pleistocene or, in most cases, entirely Holocene in age. In all but one case, vegetation cover can be assumed to have been constant and similar to that of today. The six mid-western soils are located on national prairie preserves where the vegetation shows little or no post-settlement impact. The Nevada soils come from remote mountain settings that are unsuitable for grazing, in which vegetation remains entirely native. Vegetation at the New York site, though disturbed, must always have been 100% C_3 in character given the forested nature of the region.

The isotopic composition of plants using the C_3 and C_4 photosynthetic pathways have $\delta^{13}C$ values averaging ~ -27 and -13‰, respectively[10]. We have examined ten soils the biomasses of which span the range from nearly 100% C_3 to 100% C_4 and have analysed coexisting bulk-soil organic matter and pedogenic carbonate in each. The soil carbonates were present as nodules and as pendants on pebble undersides. We confined our studies to areas where the rainfall exceeds 35 cm yr^{-1} because modelling of soils shows that pedogenic carbonate from soils with very low respiration rates, such as in deserts, can be isotopically enriched because of diffusional mixing with the atmosphere[1,11]. We sampled carbonates at depths >30 cm because the near-surface carbonate could be affected by diffusional mixing with atmospheric CO_2, irrespective of the soil respiration rate. Nearly all the soils studied contained carbonate in the parent alluvium, loess or till.

The diffusion coefficients for $^{12}CO_2$ and $^{13}CO_2$ differ, producing a 4.4‰ enrichment in the plant-derived component of soil CO_2 compared with respired CO_2 (refs 1, 11, 12). At equilibrium, the isotopic equilibrium factor $10^3 \ln \alpha_{CO_2\text{-calcite}}$ is -9.8 to -12.4 for the temperature range 25–0 °C (ref. 13). Pedogenic carbonate precipitated in equilibrium with soil CO_2 should, therefore, be $\sim$14‰ (25 °C)–17‰ (0 °C) enriched relative to respired CO_2. At low soil respiration rates, carbonates precipitated in equilibrium with soil CO_2 would have an even greater enrichment as a result of the atmospheric effects mentioned above.

The isotopic composition of pedogenic carbonate from a single soil in the Konza Prairie of Kansas is constant in the soil from depths of 40 to 103 cm, and it is 14.5‰ more positive than the co-existing organic material in the soil (Fig. 1). This difference supports the model of a diffusion-controlled soil CO_2–$CaCO_3$ system in isotopic equilibrium. The patterns displayed by this soil and those described below are not consistent with kinetic or Rayleigh distillation processes resulting in isotopic disequilibrium between soil CO_2 and precipitated carbonate. Similarly, modern soil organic matter and coexisting pedogenic carbonate from nine other North American soils differ by $\sim$14–16‰ (Fig. 2), as predicted for high-respiration-rate soils. All soils we studied, including palaeosols from Pakistan, show strong leaching and contain well developed organic horizons, thus indicating high respiration rates[14,15]. In low-respiration-rate soils, such as in deserts, diffusional mixing of atmospheric CO_2 and plant-derived CO_2 can produce up to 2‰ enrichment in the $\delta^{13}C$ of soil carbonate at 50-cm depth[11]. No systematic trend in

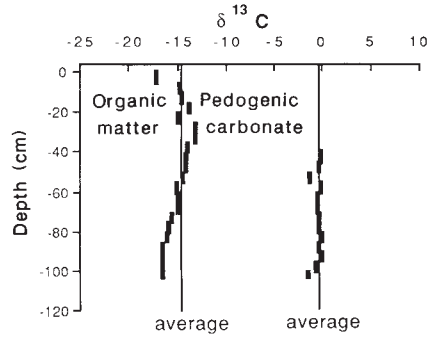

FIG. 1 The isotopic composition of soil organic matter and pedogenic carbonate as a function of depth in a prairie soil from Kansas, USA.